IEEE Access
Multidisciplinary | Rapid Review | Open Access Journal

Received January 3, 2019, accepted January 17, 2019, date of publication January 23, 2019, date of current version March 13, 2019.

Digital Object Identifier 10.1109/ACCESS.2019.2894409

A Three-Dimensional Phantom Track Generation for Radar Network Deception

XIANG LIU and DONGSHENG LI
College of Electronic Engineering, National University of Defense Technology, Hefei 230037, China
Corresponding author: Xiang Liu (liuxiang0802@126.com)

ABSTRACT One important issue when multiple cooperating electronic combat air vehicles (ECAVs) are used to generate phantom radar tracks in a radar network is the position inaccuracy, which is the fundamental reasons for the difference between a phantom track and a real track. According to this difference, a radar network can recognize the phantom track from the real target track. In order to solve this problem, first, two kinds of phantom tracks in three-dimensional space are developed from the generalized kinematic framework. Then, the effect of the inaccuracies of radar position and ECAVs position to the phantom track is considered in detail. Finally, the beam rider guidance method is used to compensate the track deviation. The scenario of phantom track generation and the influence factors of the maximum position deviation is simulated and analyzed particularly. The simulation results show that the deviation compensation method can reduce the recognition rate of the phantom track effectively.

INDEX TERMS Electronic combat air vehicles, radar network, phantom tracks, deviation compensation.

I. INTRODUCTION

Radar network system employing multiple, widely distributed stations have been shown to offer significant advantages over monostatic radar in various aspects of radar applications, such as moving target detection, direction finding and target localization, which poses a great threat to the stealth airplane, low altitude attack, and anti-radiation missile [1]–[5]. Radar phantom track generation by a group of cooperating ECAVs has received increased attention in the recent past. The phantom track can seduce the radar network to detect and track the motion of an air vehicle that does not actually exist and reduce the correct recognition rate of the target [6], [7].

The concept for generating coherent radar phantom tracks using cooperating vehicles was introduced in [8], which considered two different problems. Subsequently, the flyable ranges for an ECAV for the same class of phantom tracks were developed by Keith *et al.* [9] and generalized bounds were presented for initial conditions. Maithripala and Jayasuriya [10] presented a control algorithm for an ECAV team where kinematic constraints on the ECAV dynamic system were translated to constraints on the phantom point. The evolving phantom track in turn generated the actual controls on the ECAVs so that ECAVs had flyable trajectories. Subsequently, the authors generalized the control algorithm to three dimensions. The necessary and sufficient conditions were extended to ECAV's state, speed, and curvature constraints, and developing an algorithm capable of generating trajectories online and in real-time [11]. Recently, the optimal ECAV and coherent phantom track mission are designed considering high dimensionality and kinematic, dynamics, and geometric constraints [12]–[14].

The phantom track deception mission is of strict demands because of its cooperation and dynamics, and geometric constraints. As a result, the target parameter and the environment are often idealized and analyzed in two-dimensional (2-D), when researching on the phantom track. Developing an effective phantom track deception capability in three-dimensional (3-D) space is of interest because it is challenging scientifically [15]–[17]. Phantom target trajectories for unlimited time deception were generated by Ratnoo and Shima [18], but the kinematic relations for generating the phantom track was presented in 2-D. Beyond that, the conditions for the finite time phantom track were not addressed further. Dhananjay and Ghose [19] designed the phantom track in a vertical plane by using the projected positions of the radar locations, the radar deception problem is extended to 3-D and noncollinear radars. In this paper, we deduce the 3-D constraint condition of the control parameters for the ECAVs, then design the real-time trajectories for the different missions.

The above research mainly considers the optimal control problem of the phantom track. However, there is little

research has been done on how to maintain the survival and interference effects of the phantom track after taking countermeasures on radar network.

Another important issue of the phantom track is the effect of the position inaccuracy [20], [21]. The radar network can recognize the phantom track according to the difference in spatial distribution property between the phantom track and the target track. From the former analysis, we have known that most of the existing work has addressed the problem in ideal condition. In fact, it is inevitable that there are the inaccuracies of radar position and ECAVs position which are obtained through electronic reconnaissance.

The major contributions of this paper are mainly in the following aspects:

1. The phantom track deception mission is of strict demands because of its high dimensionality and dynamics, and geometric constraints. As a result, the target parameter and the environment are usually analyzed in (2-D) space, which can't reflect the reality. Extending these conditions for 3-D scenarios is challenging. Therefore, we take the true environment into account and build a more realistic phantom track deception scenario under complex 3-D space.
2. By analyzing the dynamic constraints of the path control parameter (PCP), the state and control vectors in the dynamics models of the phantom track generation can be represented by a single degree of freedom vector and thus eases the optimization problem. Further, it is shown that phantom tracks for specific missions like infinite time deception and finite time deception can also be generated using the proposed kinematic framework.
3. Another unaddressed issue in phantom target generation is the inevitable position inaccuracies, which is the fundamental reasons for the difference between phantom track and real track. We analyze the effect of the inaccuracies to the phantom track in detail and propose a deviation compensation for the inaccuracies. The technology of deviation compensation also makes it possible to reach a deception formation from any given initial ECAV position configuration.
4. Association testing used by centralized and distributed radar network based on the difference in spatial distribution property between the phantom track and the target track are derived. The comparative results of the association testing with/without deviation compensation control are simulated in detail at last, and the results show that the technology of deviation compensation can reduce the recognition rate of the phantom track effectively.

In my previous article [22], some methods have been proposed to solve the existing problems at present. This work extends the phantom track problem discussed in [18] to 3-D and distributed radar network.

The paper is organized as follows. Two phantom track generation methods of infinite time and finite time are proposed in Section II. In Section III, the effect of the inaccuracies of radar position and ECAVs position to the phantom track is considered, which is based on the problem formulation. The ECAV may off the desired initial position, and we need to use a beam rider guidance law [23] with lead compensation to correct its position error. Therefore, we extend the deviation compensation in [18] to 3-D, and the flight-control system using beam rider guidance commands is given in Section IV. Theoretical analysis and computer simulation justify the validity and efficiency in Section V. Finally, Section VI concludes the paper.

II. PROBLEM FORMULATION AND MODEL DESCRIPTION

A. PROBLEM FORMULATION

This paper addresses the control of a group of ECAVs generating phantom tracks to deceive a radar network. The ECAVs are stealthy and can use range delay deception to deceive a radar network. The problem is to design a realistic phantom track for radar network that ensures the existence of a feasible solution for the ECAV trajectory for the entire mission duration.

Range deception of radar network using electronic combat air vehicles is actually one of many tactics that could be employed for electronic attack (EA) in an electronic warfare (EW) scenario. ECAVs receive the pulses from the radar, storing them, and then sending back with a certain time delay so that the radar receives the false pulses and sees a phantom target at a range beyond the truth. If multiple vehicles coordinate their positions and delays, the phantom points will converge and the radar network will be deceived. Through coordinated trajectory planning, the vehicles can make this phantom point move in a phantom trajectory [19], [24].

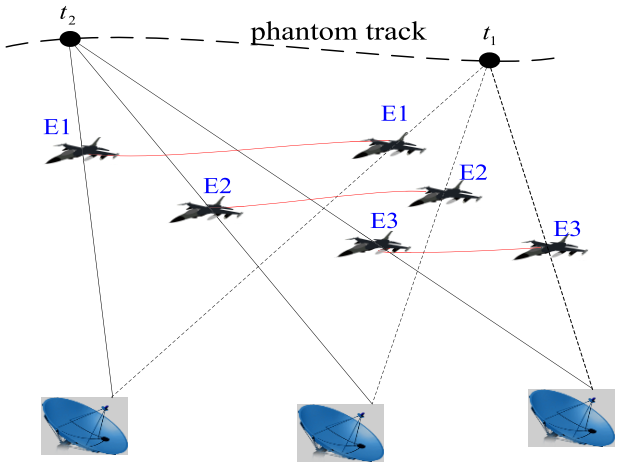

FIGURE 1. Phantom track generation through ECAVS.

Fig. 1 illustrates how three ECAVs could cooperatively create a single phantom track to deceive a network of three radars by using range-delay techniques.

The following assumptions are made in the problem formulation where the ECAVs have to meet in order to generate phantom track.

1. Each ECAV is in the line of sight (LOS) joining the corresponding radar location to the phantom position. That is to say, the creation of the phantom track is through main-lobe deception using range delay techniques.
2. ECAVs are mass-less and their states are completely observable.
3. Both the phantom track as well as the ECAVs will have constrained dynamics, and the ground radar locations are fixed.

B. PHANTOM TRACK DYNAMICS

The case of a single ECAV engaging a single radar was discussed in Dhananjay and Ghose [19], we analyze the movement of the ECAV along the LOS. We define the PCP, $p = r/R$, where r is the distance of the ECAV from the radar and R is the distance of the phantom from the same radar. In 2-D, the engagement geometry is shown in Fig. 2. Let '$\cdot$' denote the differential form of a factor.

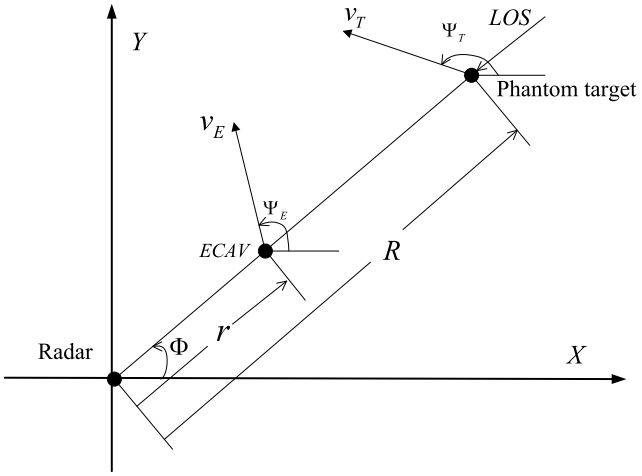

FIGURE 2. ECAV and phantom target variables in 2-D.

As the phantom target is generated along the LOS, the LOS angular rate as expressed in terms of individual ECAV and phantom target kinematics must be identical, that is

$$\dot{\Phi} = \frac{v_T \sin(\Psi_T - \Phi)}{R} = \frac{v_E \sin(\Psi_E - \Phi)}{r} \tag{1}$$

$$p = r/R, \quad 0 < p < 1 \tag{2}$$

where Φ is the LOS angle, Ψ is the course angle of ECAV or phantom target, v is the speed of ECAV or phantom target. Subscripts E and T denote ECAV and phantom target respectively. It should be noted that we only consider the situation $0 < p < 1$ for $0 < r < R$. When $p \geq 1$ for $0 < R < r$, the phantom track generation method proposed in this article is also suitable. Differentiating (2) with respect to time t, we get

$$\dot{p}R + p\dot{R} = \dot{r} = v_E \cos(\Psi_E - \Phi) \tag{3}$$

From (1), we have

$$pv_T \sin(\Psi_T - \Phi) = v_E \sin(\Psi_E - \Phi) \tag{4}$$

Squaring and adding (3) and (4), simplifying the result we can get a quadratic equation in $\dot{p}$ as

$$R^2\dot{p}^2 + 2R\dot{R}p\dot{p} + p^2v_T^2 - v_E^2 = 0 \tag{5}$$

Solving for $\dot{p}$, we have

$$\dot{p} = \frac{-p\dot{R} \pm \sqrt{(p\dot{R})^2 + K_1}}{R} \tag{6}$$

where

$$K_1 = v_E^2 - p^2v_T^2 \tag{7}$$

Now we want to extend the radar deception problem to 3-D. The engagement geometry in 3-D is shown in Fig. 3. θ and ϕ are the azimuth angle and elevation angle from radar to ECAV or to the phantom target. α and β are the heading angle and flight path angle of the velocity vector. The basic dynamic equations of the phantom target are obtained as follows

$$\begin{aligned} \dot{x}_T &= v_T \cos\beta_T \cos\alpha_T \\ \dot{y}_T &= v_T \cos\beta_T \sin\alpha_T \\ \dot{z}_T &= v_T \sin\beta_T \end{aligned} \tag{8}$$

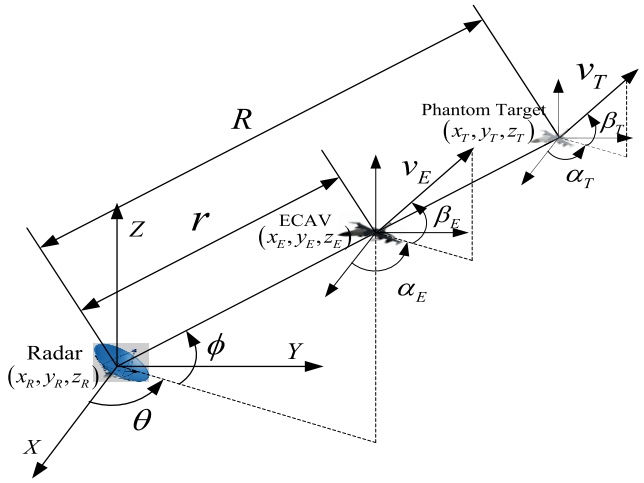

FIGURE 3. ECAV and phantom target variables in 3-D.

The equations in Cartesian coordinate transformed into the equations of motion in polar coordinate by using rotation matrix.

$$\begin{bmatrix} \dot{R} \\ R\dot{\theta}\cos\phi \\ R\dot{\phi} \end{bmatrix} = \begin{bmatrix} \cos\phi\cos\theta & \cos\phi\sin\theta & \sin\phi \\ -\sin\theta & \cos\theta & 0 \\ -\sin\phi\cos\theta & -\sin\phi\sin\theta & \cos\phi \end{bmatrix} \begin{bmatrix} \dot{x}_T \\ \dot{y}_T \\ \dot{z}_T \end{bmatrix} \tag{9}$$

Using (8) in (9) leads to

$$\dot{R} = v_T(\cos\phi\cos\theta\cos\beta_T\cos\alpha_T + \cos\phi\sin\theta\cos\beta_T\sin\alpha_T + \sin\phi\sin\beta_T)$$

$$\dot{\theta} = \frac{v_T}{R\cos\phi}(-\sin\theta\cos\beta_T\cos\alpha_T + \cos\theta\cos\beta_T\sin\alpha_T)$$
$$\dot{\phi} = \frac{v_T}{R}(-\sin\phi\cos\theta\cos\beta_T\cos\alpha_T - \sin\phi\sin\theta \times \cos\beta_T\sin\alpha_T + \cos\phi\sin\beta_T) \quad (10)$$

The equations of motion for the ECAV are similar to the phantom dynamics. According to Eq. (10), we get

$$\dot{r} = v_E(\cos\phi\cos\theta\cos\beta_E\cos\alpha_E + \cos\phi\sin\theta\cos\beta_E \times \sin\alpha_E + \sin\phi\sin\beta_E)$$
$$\dot{\theta} = \frac{v_E}{r\cos\phi}(-\sin\theta\cos\beta_E\cos\alpha_E + \cos\theta\cos\beta_E\sin\alpha_E)$$
$$\dot{\phi} = \frac{v_E}{r}(-\sin\phi\cos\theta\cos\beta_E\cos\alpha_E - \sin\phi\sin\theta\cos\beta_E \times \sin\alpha_E + \cos\phi\sin\beta_E) \quad (11)$$

According to the solution method of $\dot{p}$ in (6). Using (3), (10) and (11), the result of quadratic equation in $\dot{p}$ can be deduced that

$$\dot{p} = \frac{-p\dot{R} \pm \sqrt{(p\dot{R})^2 + K_2}}{R} \quad (12)$$

where

$$K_2 = v_E^2[(\cos\beta_E)^2(\cos(\theta-\alpha_E))^2 + (\sin\beta_E)^2] - p^2v_T^2[(\cos\beta_T)^2(\cos(\theta-\alpha_T))^2 + (\sin\beta_T)^2] \quad (13)$$

From (7) and (13), we can see that the result of $\dot{p}$ in 2-D is a special solution of the equation in 3-D. Therefore the kinematic conditions for the feasible phantom track by a group of ECAVs in 3-D will be presented especially in the next.

C. TWO GENERATING METHORDS OF PHATOM TRACKS

Time of deception is an important aspect of the mission. By analyzing (12) and (13), kinematic conditions for generating the two continuous phantom tracks are presented.

1) INFINITE TIME PHANTOM TRACK

According to (12) and (13), in order to generate an infinite time phantom track, that is, after a certain time t_0, $\dot{p} = 0$ during $0 < p < 1$. The control parameters in (12) should satisfy

$$\alpha_T = \alpha_E = \theta \quad (14)$$
$$p = v_E/v_T \quad (15)$$

(14) is used to ensure that the ECAV and phantom target are in two parallel planes. (15) is used to ensure that the two planes always maintain a certain distance. However, there is a hidden condition here because the choice of the "±" sign in (12) is related to the plus-minus sign of the $\dot{r}$. When $\dot{r} > 0$ the "+" sign in (12) will be used. When $\dot{r} < 0$ the "−" sign in (12) will be used. Therefore, in order to make $\dot{p} = 0$, the signs of $\dot{R}$ and $\dot{r}$ must be the same, i.e. the angle of the ECAV' velocity vector and the phantom target's velocity vector (relative to current LOS) are both greater than 90° or less than 90° at the same time. As a result, the parameters R and r can increase or decrease synchronously. However, when $\dot{R}$ and $\dot{r}$ are negative at the same time, r is constantly decreasing, which will lead to a collision of the ECAV with the radar. Therefore, if you want to continuously generate the phantom track, it is desirable that $\dot{R} > 0$ and $\dot{r} > 0$.

Based on the above analysis, the conditions for generating the infinite time phantom track are

$$\dot{R} > 0, \quad \dot{r} > 0, \ \alpha_T = \alpha_E = \theta, \ p = v_E/v_T \quad (16)$$

where $\dot{R} > 0, \dot{r} > 0$ is used to avoid a collision of the ECAV with the radar, $\alpha_T = \alpha_E = \theta$ is used to ensure that the ECAV and phantom target are in two parallel planes, $p = v_E/v_T$ is used to ensure that the two planes always maintain a certain distance.

2) FINITE TIME PHANTOM TRACK

In the practical application, the condition of the infinite time phantom track is pretty harsh, which is usually not necessary. Next, kinematic conditions for generating the finite time phantom track are considered.

When $\alpha_T = \alpha_E = \theta$, the solution of (12) to exist must satisfy

$$(p\dot{R})^2 - p^2v_T^2 + v_E^2 \geq 0 \Rightarrow v_E^2 \geq p^2v_T^2 - (p\dot{R})^2 \quad (17)$$

In order to prevent a collision of ECAV with phantom target or radar, the PCP should be within $0 < p_{\min} \leq p \leq p_{\max} < 1$. To always guarantee the existence of (17), a conservative speed of ECAV is chosen as

$$v_E = p_{\max}v_T \quad (18)$$

Using (14) and (18) in (12), we get

$$\dot{p} = \frac{-p\dot{R} \pm \sqrt{(p\dot{R})^2 + v_T^2\left(p_{\max}^2 - p^2\right)}}{R} \quad (19)$$

The PCP of each ECAV is monotonically increasing (or monotonically decreasing) if the "+" sign (or the "−" sign) is applied in (19). The upper and lower bound of the PCP rate are

$$\frac{-2p_{\max}\dot{R} - v_T\sqrt{\left(p_{\max}^2 - p_{\min}^2\right)}}{R} < \dot{p} \leq 0 \ \dot{R} > 0, \quad \dot{r} < 0$$
$$0 \leq \dot{p} < \frac{2p_{\max}\dot{R} + v_T\sqrt{\left(p_{\max}^2 - p_{\min}^2\right)}}{R}\dot{R} > 0, \quad \dot{r} > 0 \quad (20)$$

Because the value of PCP rate has bound, which can be used to predict a conservative estimate of how long a coherent phantom track will last based on (20) before the ECAVs reach the maximum or minimum PCPs.

Based on the above analysis, the conditions for generating the finite time phantom track are

$$0 < p_{\min} \leq p \leq p_{\max} < 1, \quad \alpha_T = \alpha_E = \theta, \ v_E = p_{\max}v_T \quad (21)$$

where $0 < p_{\min} \leq p \leq p_{\max} < 1$ is used to avoid a collision of the ECAV with phantom target or radar, $\alpha_T = \alpha_E = \theta$ is

used to ensure that the ECAV and phantom target are in two parallel planes, $v_E = p_{\max} v_T$ is used to ensure the existence of (12).

Knowing the conditions for generating a finite time phantom track, it is possible to show the major steps of a phantom track generation through controlling multiple ECAVs as follows:

Step 1: Set the radar location for each ECAV, initial velocity v_{T0} and the phantom track you want to generate.

Step 2: Determine the range of the PCP, $p_{\min} \le p \le p_{\max}$, and the initial value p_0 for each ECAV.

Step 3: Determine the initial velocity of each ECAV according to (18), and determine the initial position of each ECAV based on the initial position of the radar and the phantom target.

Step 4: Determine the plus-minus sign in (19) according to the angle between each ECAV velocity vector and the LOS. Then calculate the value of p in the process.

Step 5: Repeat update steps $1 \sim 4$. Calculate the phantom track for each ECAV until the value p exceeds its maximum or minimum range.

III. THE EFFECT OF THE INACCURACIES TO THE PHANTOM TRACK

In reality, there are two inaccuracies will be introduced to the phantom track, which are the radar position error and the ECAVs position error. These inaccuracies contribute to a region of uncertainty around a "nominal" phantom target where the target may actually be placed by an unsuspecting ECAV. If the region is too large, then radars correlating tracks in a radar network may be able to discriminate between their respectively observed phantom targets and determine the track to be false. The above is the principle that the radar network used to identify the phantom track from the real target track.

Before generating a phantom target, it is necessary for ECAVs to reconnoiter the radars' location and pre-set the position of each ECAVs. Compared with the real target, the phantom target track mainly introduces the position inaccuracy in the following two sources.

1. The radar position error Δrd is introduced during the pre-reconnaissance process, that is, there will be a random error in the radar location obtained by reconnaissance aircraft and the actual radar location.
2. When a team of ECAVs is used to generate a phantom track, there will be a random error Δr in the actual position and the pre-set position of each ECAVs.

A. THE EFFECT OF THE INACCURACIES OF RADAR POSITION TO THE PHANTOM TARGETS

Consider the case of two ECAVs generate a phantom track to deceive two radars in the network. Fig. 4 illustrates the effect of the inaccuracies of radar position and ECAVs position to the phantom targets.

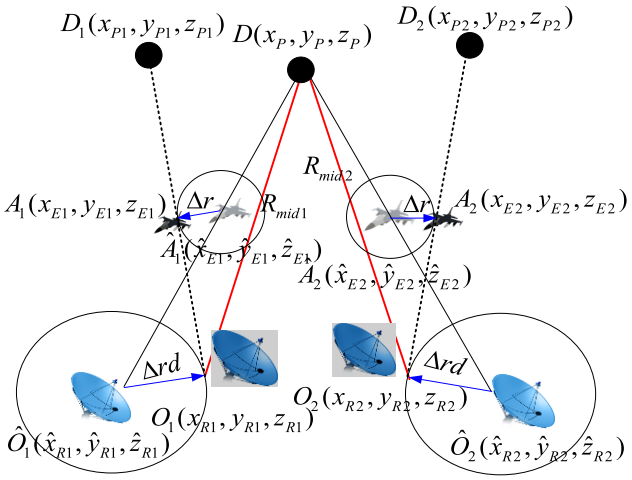

FIGURE 4. Effect of the inaccuracies to the phantom targets' position.

Let $\hat{O}_1(\hat{x}_{R1}, \hat{y}_{R1}, \hat{z}_{R1})$, $\hat{O}_2(\hat{x}_{R2}, \hat{y}_{R2}, \hat{z}_{R2})$ be the radar positions detected by the ECAVs with reconnaissance error. The two radars' actual positions are $O_1(x_{R1}, y_{R1}, z_{R1})$, $O_2(x_{R2}, y_{R2}, z_{R2})$. The two ideal ECAVs is located at $\hat{A}_1(\hat{x}_{E1}, \hat{y}_{E1}, \hat{z}_{E1})$, $\hat{A}_2(\hat{x}_{E2}, \hat{y}_{E2}, \hat{z}_{E2})$, and the actual positions of the ECAVs are $A_1(x_{E1}, y_{E1}, z_{E1})$, $A_2(x_{E2}, y_{E2}, z_{E2})$. $D(x_P, y_P, z_P)$ is the ideal phantom target position. Given an inaccuracy in radar position, Δrd, an inaccuracy in ECAV position, Δr, the "nominal" phantom target D splits into $D_1(x_{P1}, y_{P1}, z_{P1})$ and $D_2(x_{P2}, y_{P2}, z_{P2})$. Referring to Fig. 3, at a certain time k, assume that R_{mid1}, ϕ_{mid1}, θ_{mid1} are the distance, azimuth angle and elevation angle from the "nominal" phantom target D to radar1's actual position O_1. The inaccuracies contribute to the phantom target D, and the $D_1(x_{P1}, y_{P1}, z_{P1})$ in Cartesian coordinates can be expressed in radar1's actual positions O_1 as follows

$$\begin{cases} x_{P1} = (R_{mid1} + \Delta R_1)\cos(\phi_{mid1} + \Delta\phi_1) \\ \qquad \times \cos(\theta_{mid1} + \Delta\theta_1) + x_{R1} \\ y_{P1} = (R_{mid1} + \Delta R_1)\cos(\phi_{mid1} + \Delta\phi_1) \\ \qquad \times \sin(\theta_{mid1} + \Delta\theta_1) + y_{R1} \\ z_{P1} = (R_{mid1} + \Delta R_1)\sin(\phi_{mid1} + \Delta\phi_1) + z_{R1} \end{cases} \tag{22}$$

where ΔR_1, $\Delta\theta_1$, $\Delta\phi_1$ denote the position deviations in range, azimuth angle and elevation angle between D and D_1 respectively. Similarly, the $D_2(x_{P2}, y_{P2}, z_{P2})$ in Cartesian coordinates can be expressed in radar2's actual positions O_2 as follows

$$\begin{cases} x_{P2} = (R_{mid2} + \Delta R_2)\cos(\phi_{mid2} + \Delta\phi_2) \\ \qquad \times \cos(\theta_{mid2} + \Delta\theta_2) + x_{R2} \\ y_{P2} = (R_{mid2} + \Delta R_2)\cos(\phi_{mid2} + \Delta\phi_2) \\ \qquad \times \sin(\theta_{mid2} + \Delta\theta_2) + y_{R2} \\ z_{P2} = (R_{mid2} + \Delta R_2)\sin(\phi_{mid2} + \Delta\phi_2) + z_{R2} \end{cases} \tag{23}$$

where ΔR_2, $\Delta\phi_2$, $\Delta\theta_2$ denote the position deviations in range, azimuth angle and elevation angle between D and D_2 respectively. The effect of the inaccuracies of radar position

and ECAVs position to the phantom targets can be measured by the distances between D_1 and D_2 as follows

$$d_{12} = \sqrt{(x_{P1} - x_{P2})^2 + (y_{P1} - y_{P2})^2 + (z_{P1} - z_{P2})^2} \quad (24)$$

B. ASSOCIATION TESTING

Radar network is a typical multisensor system, which can be divided into two basic fusion architectures [25], [26]: centralized and decentralized/distributed, depending on whether raw data are used directly for fusion or not.

In centralized radar network, all raw measurements are sent to the fusion center. Fig. 5 shows the configuration for the centralized radar network architecture. Centralized fusion of the measurements from all sensors at a single fusion node is theoretically optimal because the information contained in the measurements is not degraded by any intermediate processing. However, sending raw measurements needs more communication bandwidth, computation, and power consumption. Consequently, centralized fusion has a poor survivability of the system (in particular, in a war situation).

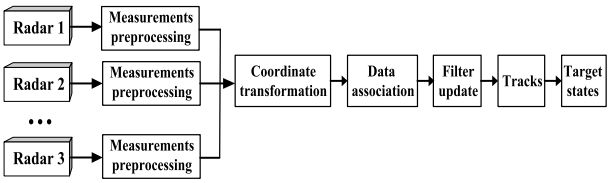

FIGURE 5. Block diagram of the centralized radar network fusion architecture.

In fig. 5, the measurements from the various radars (assumed that the measurements have been preprocessed, i.e., the radars are assumed synchronized, the outliers are eliminated, etc.) are first processed by coordinate transformation. Next, the main problem that the centralized radar network needs to deal with is the data association. In this process period, the same source testing will be used to identify the real/false target. Only the data passed the testing will be used to multi-target tracking.

It is assumed the ith radar is located at $(x_{Ri}, y_{Ri}, z_{Ri})(i = 1, 2)$. The target is located at (R_i, θ_i, ϕ_i), R_i, θ_i and ϕ_i are the distance, azimuth angle and elevation angle measured by the ith radar. The target in Cartesian coordinates can be written as follows

$$\begin{cases} x_{Pi} = R_i \cos\theta_i \cos\phi_i + x_{Ri} \\ y_{Pi} = R_i \sin\theta_i \cos\phi_i + y_{Ri} \\ z_{Pi} = R_i \sin\phi_i + z_{Ri} \end{cases} \quad (25)$$

Differentiating Eq. (25)

$$\begin{bmatrix} dx_{Pi} \\ dy_{Pi} \\ dz_{Pi} \end{bmatrix} = \mathbf{A}_i \begin{bmatrix} dR_i \\ d\theta_i \\ d\phi_i \end{bmatrix} \quad (26)$$

where

$$\mathbf{A}_i = \begin{bmatrix} \cos\theta_i\cos\phi_i & -R_i \sin\theta_i\cos\phi_i & -R_i \cos\theta_i\sin\phi_i \\ \sin\theta_i\cos\phi_i & R_i \cos\theta_i\cos\phi_i & -R_i \sin\theta_i\sin\phi_i \\ \sin\theta_i & 0 & R_i\cos\phi_i \end{bmatrix} \quad (27)$$

In Eq. (26) dR_i, $d\theta_i$ and $d\phi_i$ are the distance error, azimuth angle and elevation angle error of the ith radar, which obey Gaussian distributions with zero-mean. And σ_{ri}^2, $\sigma_{\theta i}^2$ and $\sigma_{\phi i}^2$ are the variance of them respectively.

According to the property of variance

$$\mathrm{var}(\sum_{i=1}^{n} c_i\xi_i) = c_i^2 \mathrm{var}(\sum_{i=1}^{n} \xi_i) \quad (28)$$

The error matrix $[dx_{Pi}\ dy_{Pi}\ dz_{Pi}]^T$ also obeys Gaussian distributions with zero-mean, and its covariance matrix is given as below

$$\mathbf{Q}_i = \mathbf{A}_i \begin{bmatrix} \sigma_{ri} & 0 & 0 \\ 0 & \sigma_{\theta i} & 0 \\ 0 & 0 & \sigma_{\phi i} \end{bmatrix} \mathbf{A}_i^T \quad (29)$$

The correlation covariance matrix of the difference of the measurements can be expressed by

$$\begin{bmatrix} x_{P1} - x_{P2} \\ y_{P1} - y_{P2} \\ z_{P1} - z_{P2} \end{bmatrix} = \mathbf{Q}_{12} = \mathbf{Q}_1 + \mathbf{Q}_2 = \mathbf{B}\Lambda\mathbf{B}^T = \mathbf{B} \begin{bmatrix} \lambda_1 & 0 & 0 \\ 0 & \lambda_2 & 0 \\ 0 & 0 & \lambda_3 \end{bmatrix} \mathbf{B}^T \quad (30)$$

where $\mathbf{B}$ is an orthogonal matrix, λ_1, λ_2 and λ_3 are the eigenvalues of the matrix, $\lambda_1 > \lambda_2 > \lambda_3$.

Defining the adaptive threshold of the same source testing as below [22]

$$G = G_c\sqrt{\lambda_1} \quad (31)$$

where G_c is the coefficient of the adaptive threshold.

The same source testing used by centralized radar network can be designed as

$$H = \begin{cases} 1 & d_{12} < G \\ 0 & d_{12} > G \end{cases} \quad (32)$$

where 1 means from the same target, 0 means from the different targets.

In a distributed radar network, each sensor sends processed measurements to the fusion center. There are many attractive properties of such distributed systems compare with centralized radar network, including:

1. Distributed radar network is reliable in the sense that the loss of a subset of nodes and/or links does not necessarily prevent the rest of the radar network from functioning.
2. Distributed radar network is flexible in the sense that nodes can be added or deleted by making only local changes to the radar network.
3. Distributed radar network needs less communication bandwidth and computation.

Fig. 6 shows the configuration for the distributed radar network architecture.

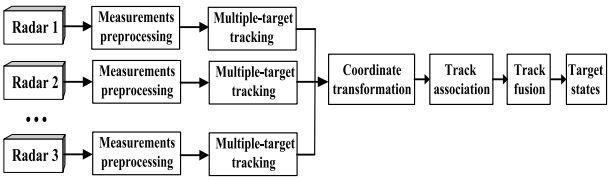

FIGURE 6. Block diagram of the distributed radar network fusion architecture.

In fig. 6, Distributed radar network transforms the tracks of radar network to fusion center and completing the time-space alignment. Then, track association testing is made for different types of track in the fusion center of the radar network. Finally, the tracks passed the inspection are fused.

In the distributed radar network, at a certain time k, we assume that the true state values of the target measured by the radar i and radar j are $\mathbf{X}^i(k)$, $\mathbf{X}^j(k)$, respectively. And the estimated state values are $\hat{\mathbf{X}}^i(k)$ and $\hat{\mathbf{X}}^j(k)$. The state estimation errors of the air target measured by the two radars can be written as

$$\tilde{\boldsymbol{X}}^i(k) = \boldsymbol{X}^i(k) - \hat{\boldsymbol{X}}^i(k) \tag{33}$$

$$\tilde{\boldsymbol{X}}^j(k) = \boldsymbol{X}^j(k) - \hat{\boldsymbol{X}}^j(k) \tag{34}$$

The difference in the true state values of the target is

$$\boldsymbol{\Delta X}^{ij}(k) = \boldsymbol{X}^i(k) - \boldsymbol{X}^j(k) \tag{35}$$

The difference in the estimated state values of the target is

$$\Delta\hat{\boldsymbol{X}}^{ij}(k) = \hat{\boldsymbol{X}}^i(k) - \hat{\boldsymbol{X}}^j(k) \tag{36}$$

The correlation test can be designed as

$$\begin{cases} H_0 : \Delta\mathbf{X}^{ij}(k) = 0, & \text{same target} \\ H_1 : \Delta\mathbf{X}^{ij}(k) \neq 0, & \text{different target} \end{cases} \tag{37}$$

The parameter $\boldsymbol{\alpha}_{ij}(k)$ is defined as

$$\boldsymbol{\alpha}_{ij}(k) = \Delta\boldsymbol{X}^{ij}(k) - \Delta\hat{\boldsymbol{X}}^{ij}(k) = \tilde{\boldsymbol{X}}^i(k) - \tilde{\boldsymbol{X}}^j(k) \tag{38}$$

Assume that the state estimation errors of the same target measured by the two radars are statistical independence, the mean value of $\boldsymbol{\alpha}_{ij}(k)$ is 0, and its covariance is

$$\boldsymbol{c}^{ij}(k) = E[\boldsymbol{\alpha}_{ij}(k)\boldsymbol{\alpha}_{ij}(k)^T] = \boldsymbol{c}^i(k) + \boldsymbol{c}^j(k) \tag{39}$$

where $\boldsymbol{c}^i(k)$ and $\boldsymbol{c}^j(k)$ are the covariance of the state estimation errors measured by radar i and radar j for the target. Its true value can't be obtained but can be replaced by the estimated value.

Define the association distance as follows

$$D_{ij} = \boldsymbol{\alpha}_{ij}(k)[\boldsymbol{c}^{ij}(k)]^{-1}\boldsymbol{\alpha}_{ij}(k)^T \tag{40}$$

The track association testing used by distributed radar network [16] can be designed as

$$\begin{cases} D_{ij} \leq D_\alpha, & \text{accept } H_0 \\ D_{ij} > D_\alpha, & \text{accept } H_1 \end{cases} \tag{41}$$

Assume under the Gaussian threshold $D_\alpha = \chi^2_{n_z}(1-\alpha)$, where α is the false alarm probability, and n_Z is the degree of freedom.

Distributed radar networked uses statistic double threshold for track association testing. In the first threshold, after the time-space alignment, M equal-length state samples in radar i and radar j are tested in (41). If the association distance D_{ij} is less than the threshold, H_0 holds. Then the counter will add 1 in the second threshold, otherwise the counter value stays the same. When the number of M state samples accepting H_0 reaches N, the samples are determined to be from the same track. The value of N/M can be 3/4, 4/5, 7/10, etc.

C. THE EFFECT OF THE INACCURACIES OF RADAR POSITION AND ECAVS POSITION TO THE FALSE TARGETS POSITION

From the previous analysis, it is known that the fundamental reason whether the phantom track can pass the correlation test is the splitting degree of the false target. The larger d_{12} is, the easier for the radar to identify the phantom track. For a fixed radar network, which does not make contributions to the change of d_{12}. The following is a brief analysis of distance d_{12} in (24). Assume the position error of the radar1 and radar2 are the same constant, and

$$x_{R1} - x_{R2} = y_{R1} - y_{R2} = z_{R1} - z_{R2} = e \tag{42}$$

Substituting (22), (23), (42) into (24), squaring the result, we get

$$\begin{aligned} d_{12}^2 = {} & R_1^2 + R_2^2 + 3e^2 + 2eR_1[\sqrt{2}\cos(\phi_1)\sin(\theta_1 + \pi/4) \\ & + \sin(\phi_1)] - 2eR_2[\sqrt{2}\cos(\phi_2)\sin(\theta_2 + \pi/4) + \sin(\phi_2)] \\ & - 2R_1R_2[\cos(\phi_1)\cos(\phi_2)\cos(\theta_1 - \theta_2) \\ & + \sin(\phi_1)\sin(\phi_2)] \end{aligned} \tag{43}$$

From the (43), we can see that the distance d_{12} is related to the distance R_i, azimuth angle θ_i and elevation angle ϕ_i from the phantom target position D_i to radar position O_i ($i = 1, 2$). The value of d_{12} increases as the distance R_i increases. When $\theta_1 > \theta_2$, the value of d_{12} increases as $\theta_1 - \theta_2$ increases. When $\theta_1 < \theta_2$, the value of d_{12} increases as $\theta_2 - \theta_1$ increases. The effect of elevation angle on the d_{12} is similar to the azimuth angle. Consider the case where d_{12} takes the maximum value, at this time, R_i, θ_i, ϕ_i should take the maximum value, only the signs are different. The maximum value of d_{12} is determined by the distance deviation ΔR, azimuth angle deviation $\Delta\theta$ and elevation angle deviation $\Delta\phi$.

Next, the maximum values of ΔR, $\Delta\theta$ and $\Delta\phi$ due to the position inaccuracies are analyzed respectively. It should be noted that the maximum distance deviation and the maximum angle deviation usually cannot be obtained at the same time. We analyze the worst case in this article, the purpose is to provide guidance for 3-D phantom track generation.

Fig. 7 below shows the radar/ECAV configuration where the maximum positive distance deviation occurs.

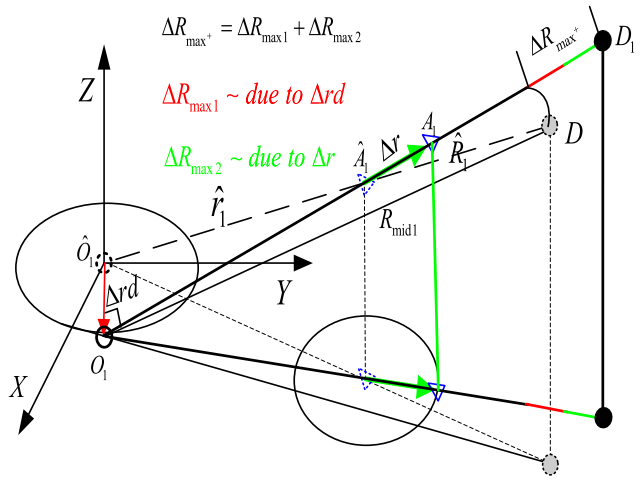

FIGURE 7. Radar/ECAV locations and geometry required to produce ΔR_{max+}.

From Fig. 7, we can see that the maximum distance deviation

$$\Delta R_{\max^+} = \Delta R_{\max 1} + \Delta R_{\max 2} \tag{44}$$

To radar1/ECAV1, the ECAV sends the pulses back with a certain time delay, which will produce the same delay distance at a time, that is

$$A_1D_1 = \hat{A}_1D = \hat{R}_1 - \hat{r}_1 \tag{45}$$

where $\hat{R}_1$ is the distance of $D\hat{O}_1$, $\hat{r}_1$ is the distance of $\hat{A}_1\hat{O}_1$, we have

$$\Delta R_{\max 1} = \sqrt{\hat{r}_1^2 - \Delta rd^2} + (\hat{R}_1 - \hat{r}_1) - R_{mid1} \tag{46}$$

$$\Delta R_{\max 2} = \Delta r \tag{47}$$

where R_{mid1} is the distance of DO_1, which can be derived using the law of cosines in $\Delta\hat{O}_1O_1D$

$$R_{mid1} = \sqrt{\hat{R}_1^2 + \Delta rd^2 - 2\hat{R}_1\Delta rd\frac{\Delta rd}{\hat{r}_1}} \tag{48}$$

Radar2/ECAV2 has similar equations as deduced above, the derivation process is omitted here.

Fig. 8 below shows the radar/ECAV configuration where the maximum positive azimuth angle deviation occurs.

From the Fig. 8, we can see that the maximum positive azimuth angle deviation

$$\Delta\theta_{\max^+} = \Delta\theta_{\max 1} + \Delta\theta_{\max 2} \tag{49}$$

where

$$\Delta\theta_{\max 1} = \arcsin\left(\frac{r_{mid}\Delta rd(\hat{R}_1 - \hat{r}_1)}{R_{mid1}\hat{r}_1\sqrt{\Delta r^2 + r_{mid}^2}}\right) \tag{50}$$

$$\Delta\theta_{\max 2} = \arctan\frac{\Delta r}{r_{mid}} \tag{51}$$

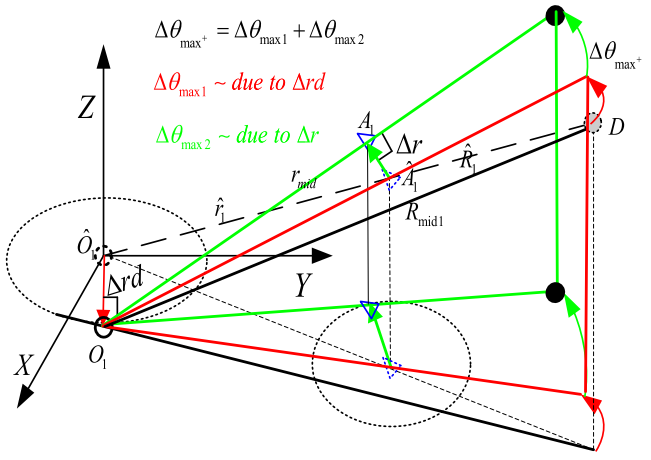

FIGURE 8. Radar/ECAV locations and geometry required to produce $\Delta\theta_{max+}$.

where r_{mid} is the distance of O_1A_1, $\Delta\theta_{\max 1}$ can be derived using the law of sines in $\Delta O_1D\hat{A}_1$ and $\Delta D\hat{O}_1O_1$

$$\frac{(\hat{R}_1 - \hat{r}_1)}{\sin\Delta\theta_{\max 1}} = \frac{\sqrt{\Delta r^2 + r_{mid}^2}}{\sin\angle O_1D\hat{A}_1} \tag{52}$$

$$\frac{\Delta rd}{\sin\angle O_1D\hat{A}_1} = \frac{R_{mid1}}{\sin\angle D\hat{O}_1O_1} \tag{53}$$

$$\sin\angle D\hat{O}_1O_1 = \frac{r_{mid}}{\hat{r}_1} \tag{54}$$

$$r_{mid} = \sqrt{\hat{r}_1^2 - (\Delta rd^2 + \Delta r^2)} \tag{55}$$

Using (52) ~(55), the result of $\Delta\theta_{\max 1}$ in (50) can be deduced.

Radar2/ECAV2 has the similar equations as deduced above, but produces the maximum negative deviation in azimuth angle, the derivation process is omitted here.

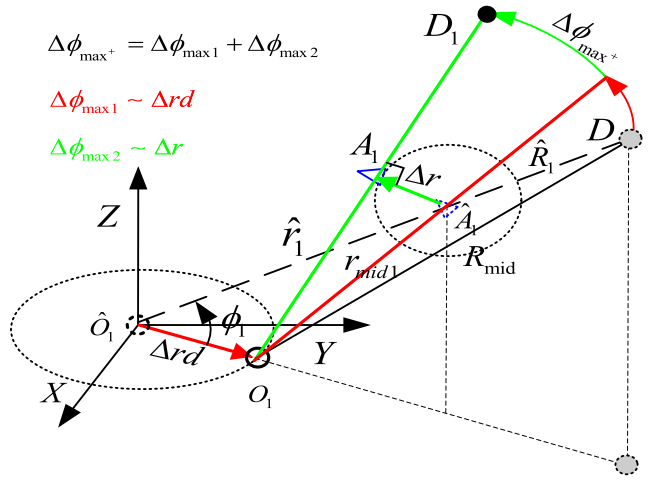

FIGURE 9. Radar/ECAV locations and geometry required to produce $\Delta\phi_{max+}$.

Fig. 9 below shows the radar/ECAV configuration where the maximum positive elevation angle deviation occurs.

From the Fig. 9, we can see that the maximum positive elevation angle deviation

$$\Delta\phi_{\max+} = \Delta\phi_{\max 1} + \Delta\phi_{\max 2} \tag{56}$$

where

$$\Delta\phi_{\max 1} = \arccos\left(\frac{R_{mid1}^2 + r_{mid1}^2 - (\hat{R}_1 - \hat{r}_1)^2}{2R_{mid1}r_{mid1}}\right) \tag{57}$$

where r_{mid1} is the distance of $O_1\hat{A}_1$. Using the law of cosines in $\Delta\hat{O}_1O_1D$ and $\Delta\hat{O}_1O_1\hat{A}_1$, we have

$$r_{mid1} = \sqrt{\hat{r}_1^2 + \Delta rd^2 - 2\hat{r}_1\Delta rd\cos\phi_1} \tag{58}$$

$$R_{mid1} = \sqrt{\hat{R}_1^2 + \Delta rd^2 - 2\hat{R}_1\Delta rd\cos\phi_1} \tag{59}$$

$$\Delta\phi_{\max 2} = \arcsin\frac{\Delta r}{r_{mid1}} \tag{60}$$

Radar2/ECAV2 has the similar equations as deduced above, but produces the maximum negative deviation in elevation angle, simply replace ϕ_1 with $\pi - \phi_1$ in the formulas above.

IV. DEVIATION COMPENSATION FOR THE INACCURACIES

From Section III, we can see that the deviation compensation should include two parts: distance deviation compensation and angle deviation compensation. In fact, the angle deviation contributes much more to distance d_{12} than the distance deviation, the latter simulation can verify this conclusion. In addition, the distance deviation can be compensated by increasing or reducing the time delay of ECAVs, which is relatively easy. This section focuses on the compensation control method for the angle deviation.

Assume θ_T, ϕ_T are the azimuth angle and elevation angle from the phantom target to radar, θ_E, ϕ_E are the azimuth angle and elevation angle from ECAV to radar. Fig.10 below shows the ECAV is off the desired phantom target LOS angle respect to the radar.

From Fig. 10 the angle deviations ε_1 and ε_2 of the ECAV due to the azimuth and elevation angle deviations respectively can be defined as

$$\varepsilon_1 = \theta_T - \theta_E \tag{61}$$

$$\varepsilon_2 = \phi_T - \phi_E \tag{62}$$

The values of the angle deviation are generally small, so the position deviations l_1, l_2 relative to ε_1, ε_2 can be approximated as

$$l_1 = r\cos\phi_T(\theta_T - \theta_E) \tag{63}$$

$$l_2 = r(\phi_T - \phi_E) \tag{64}$$

As discussed in [18], the beam rider guidance law [23] can be used to bring the actual ECAVs back onto the LOS. The simplest possible implementation of a guidance law for a beam rider system is to make the ECAV lateral acceleration commands proportional to the position deviation as

$$\hat{a}_{E1} = k_1 l_1 = k_1 r\cos\phi_T(\theta_T - \theta_E) \tag{65}$$

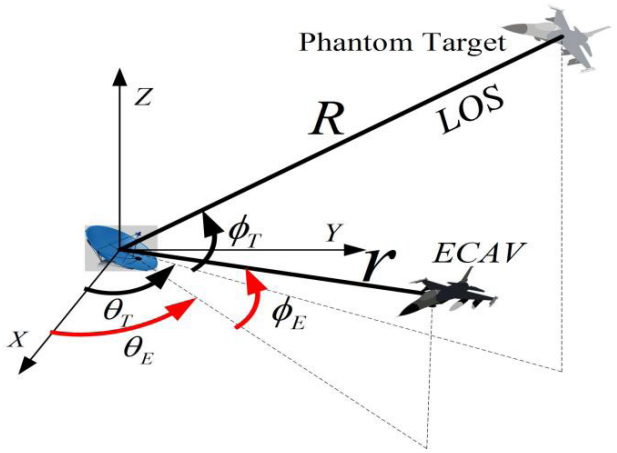

FIGURE 10. Radar/ECAV locations and geometry with the inaccuracies θ_E/ϕ_E.

$$\hat{a}_{E2} = k_2 l_2 = k_2 r(\phi_T - \phi_E) \tag{66}$$

where k_1, k_2 are the guidance gains, in order to avoid an oscillatory response, the lead compensator $G(s)$ is used for beam rider implementation as

$$a_{E1} = k_1 G(s) r\cos\phi_T(\theta_T - \theta_E) \tag{67}$$

$$a_{E2} = k_2 G(s) r(\phi_T - \phi_E) \tag{68}$$

$$G(s) = \frac{1 + s/a}{1 + s/b} \tag{69}$$

where a and b are positive constants, with b chosen to be about one order of magnitude higher than a.

Note that we use the position deviation instead of the angle deviation to form the lateral acceleration commands. The reason is that if the angle deviation ε_1 and ε_2 are constants, the distance of the ECAV from the LOS is also different with the change of the distance r.

Block diagram of the flight-control system using beam rider guidance commands is shown in Fig. 11.

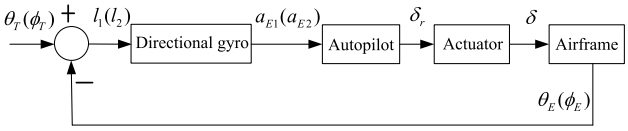

FIGURE 11. Block diagram of the flight-control system.

The purpose of the flight-control system, shown in Fig. 11, is to convert the ECAV's acceleration command a_E generated by the beam rider guidance law to an achieved acceleration of the airframe. The ECAV airframe is a controlled object in the flight-control system. In this flight-control system, the directional gyro measures the angles of the ECAV and feeds back this information to develop an error signal. The directional gyro then develops the error signal into a lateral acceleration command. The autopilot is another part of the flight-control system and is the mechanism for converting the

acceleration command a_E to a fin deflection command δ_r. The actuator then takes the autopilot's electrical output command and moves the ECAV control surfaces (that is, canards, wings, or tails) through the appropriate angular deflection δ in response to the fin deflection command.

To illustrate the working process of the flight-control system, we consider an azimuth angle deviation compensation example. The simplest case is that the position deviation $l_1 = 0$, that is, ECAV is always on the LOS between the radar and the phantom target. Therefore $a_E = 0$, there is no fin deflection command to the actuator and the ECAV control surfaces do not move. Assuming that the position deviation $l_1 > 0$ (ECAV is on the right of the phantom target as shown in Fig. 10), to minimize l_1 the directional gyro measures the azimuth angle then develops the error signal into a lateral acceleration command a_{E1}. The actuator then takes the autopilot's fin deflection command and moves the ECAV control surfaces swinging to the left, thus producing a moment $M_1(\delta_r)$ that drives the ECAV back to the LOS. As the position deviation decreases, the control signal a_{E1} also decreases. When the servo feedback signal exceeds a_{E1}, the servo input signal will change polarity, and the ECAV will return to the original equilibrium position again. If the position inaccuracy disappears, the deviation compensation process ends.

V. SIMULATION RESULTS

In this section, we assume radars are located at (5 km, −20 km, 0 km), (60 km, −15 km, 0 km), respectively. The initial phantom target is located at (25 km, −6 km, 3 km), with its airspeed (200 m/s, 100 m/s, 10 m/s). The measurement accuracy of a radar system is the degree of closeness of measurements of a quantity to that quantity's actual (true) value . Although there are many factors affect the measurement accuracy of a radar system, it is generally considered that the radar's measurement error obeys the zero-mean Gaussian distribution without considering the system error. The two radars have the same measurement accuracy. 50 m, 0.8°, 0.8° are the standard deviation of distance, azimuth angle, and elevation angle measurement error respectively. The PCP of ECAV1 $0.3 < p_1 < 0.8$, and its initial value $p_{10} = 0.6$. The PCP of ECAV2 $0.35 < p_2 < 0.85$, and its initial value $p_{20} = 0.75$.

A. PHANTOM TRACK GENERATION

From Fig. 12 and Fig. 13, it can be seen that the two ECAVs can generate a cooperative phantom track continuously. As the distance from ECAV1 to Radar 1 increases, its PCP also increases. ECAV2/Radar2 has an opposite case. The time-varying properties of individual ECAVs' parameters are shown in Fig. 14. We can see that the changes of individual ECAVs' deception distance are consistent with the variation of their PCPs. It is easy to understand, according to Eq. (2), there is a positive correlation between the deception distance and PCP. The changes of individual ECAVs' azimuth angle and elevation angle are related to individual ECAVs' airspeed.

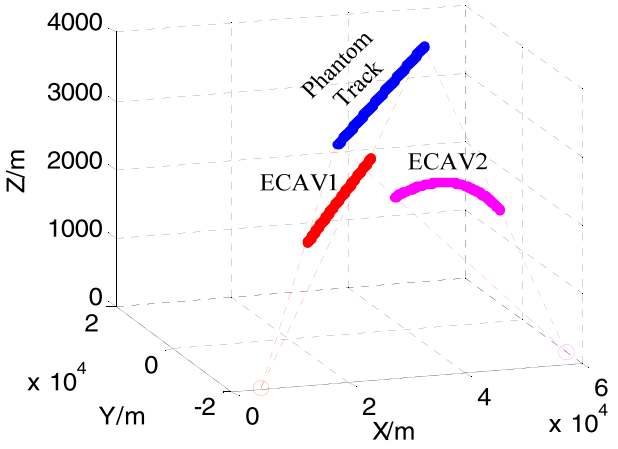

FIGURE 12. ECAVs and phantom tracks.

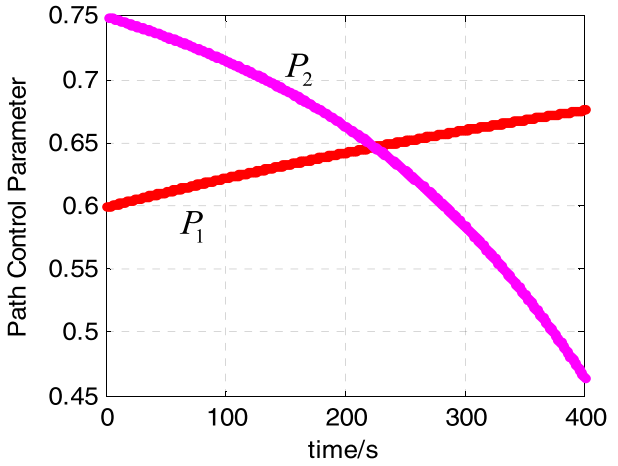

FIGURE 13. Variation of the PCPs.

The simulation results are consistent with the analysis in Section II.

B. ANALYSIS OF THE INFLUENCE FACTORS OF THE MAXIMUM POSITION DEVIATION

Given an inaccuracy in ECAV position $\Delta r = 50\ m$, an inaccuracy in radar position $\Delta rd = 60\ m$. R, r are the distance from the phantom target and ECAV to radar, respectively. Fig. 15 shows the variations of the maximum distance and angle deviation with the changes of R and r.

From Fig. 15 (a) to (c), it can be seen that the variations of the $\Delta R_{\max}$, $\Delta\theta_{\max}$, $\Delta\phi_{\max}$ mainly have a positive correlation with R and a negative correlation with r. However, the changes of R and r mainly affect the result of angle deviation, and there are almost no contribution to the distance deviation.

Assume that the distance from the phantom target and ECAV to radar are constant, i.e. $r = 25\ km$, $R = 35\ km$. The range for inaccuracy in ECAV position Δr within [25 m, 65 m], The range for inaccuracy in radar position Δrd within [35 m, 75 m]. Fig. 16 shows the variations of the

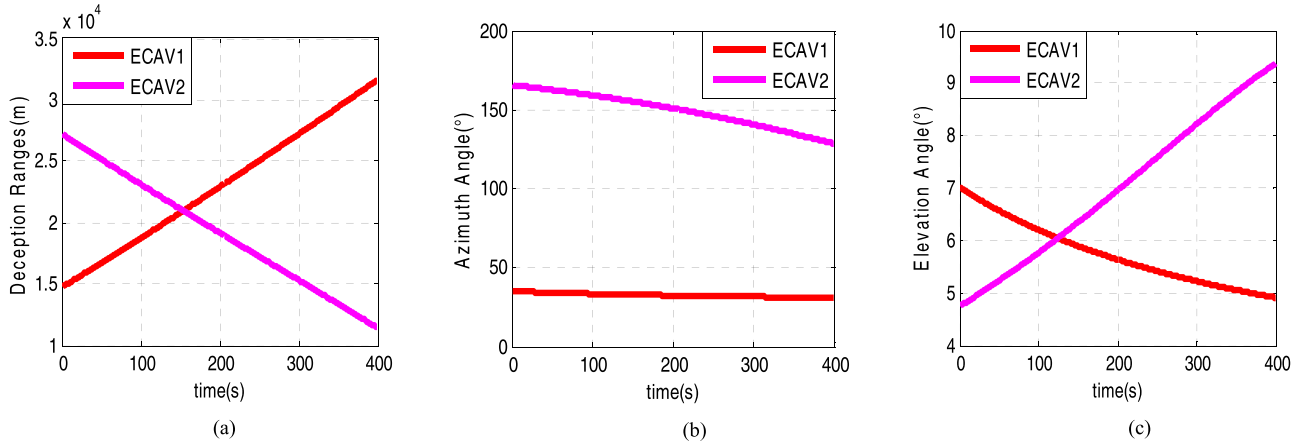

FIGURE 14. The time-varying properties of individual ECAVs' parameters. (a) Variations of the deception distance. (b) Variations of the azimuth angle. (c) Variations of the elevation angle.

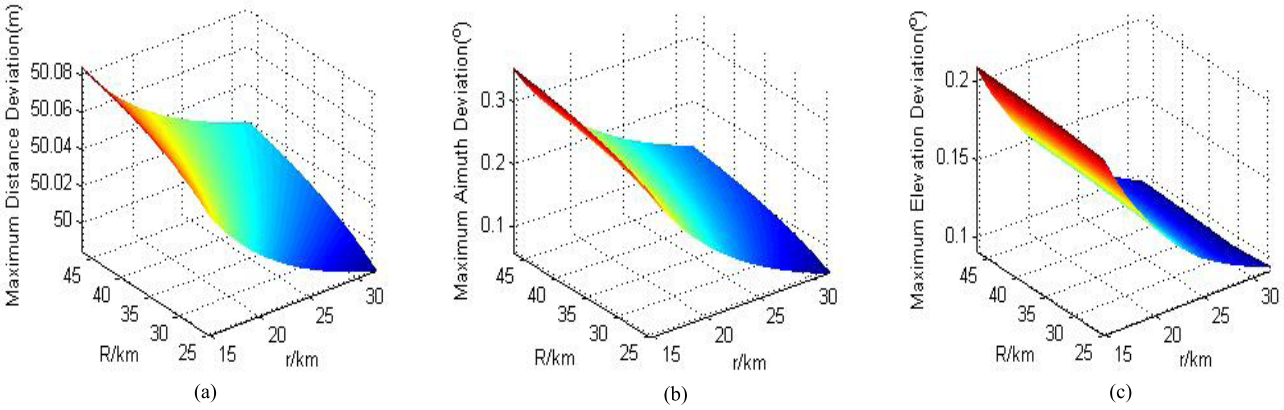

FIGURE 15. Variations of the $\Delta R_{\max}$, $\Delta\theta_{\max}$, $\Delta\phi_{\max}$ with the changes of R and r. (a) Variations of the $\Delta R_{\max}$. (b) Variations of the $\Delta\theta_{\max}$. (c) Variations of the $\Delta\phi_{\max}$.

maximum distance and angle deviation with the changes of Δr and Δrd.

From Fig. 16 (a) to (c), it can be seen that the variations of the $\Delta R_{\max}$, $\Delta\theta_{\max}$, $\Delta\phi_{\max}$ mainly have a positive correlation with the changes of Δr and Δrd. Furthermore, $\Delta R_{\max}$, $\Delta\theta_{\max}$, $\Delta\phi_{\max}$ are mainly determined by the value of Δr.

Next, considers the influence of inaccuracy y in position on d_{12}. Three simulation scenarios are considered.

(a) Only has the inaccuracy in ECAV position $\Delta r = 50\,m$.
(b) Only has the inaccuracy in radar position $\Delta rd = 60\,m$.
(c) Given the two inaccuracies in ECAV and radar positions, i.e. $\Delta r = 50\,m$, $\Delta rd = 60\,m$.

Fig. 17 shows the variations of d_{12} with the time in the three scenarios above.

From the results in Fig. 17, it can be seen that associated distance d_{12} is getting bigger and bigger with the increase of time. Comparing Fig. 17 (a) with Fig. 17 (b), we can see that the contribution Δr to d_{12} is greater than Δrd. Comparing Fig. 17 and Fig. 15, it can be seen that the increase of d_{12} is mainly determined by the angle deviation.

C. THE EFFECT OF THE DEVIATION COMPENSATION TO THE ANGLE DEVIATION

Given an inaccuracy in ECAV position $\Delta r = 50\,m$, an inaccuracy in radar position $\Delta rd = 60\,m$. Using the method in Section IV to add lateral acceleration control commands to ECAV, the guidance gain $k_1 = k_2 = 10$, the lead compensator $G(s) = (1 + s/2)/(1 + s/20)$.

Fig. 18 is the simulation results for the case when ECAV violates the LOS angle constraint. The azimuth angle of ECAV is slightly offset from the LOS. The result shows that the beam rider guidance law can drive the ECAV back to the LOS quickly. The deviation compensation to the elevation angle has the similar simulation result as shown above, the simulation process is omitted here.

D. THE EFFECT OF THE DEVIATION COMPENSATION TO THE ASSOCIATION DETECTION

In this section, assume that the range for inaccuracy in ECAV position Δr within $[25\,m, 55\,m]$, the range for inaccuracy in radar position Δrd within $[35\,m, 65\,m]$. The Gaussian

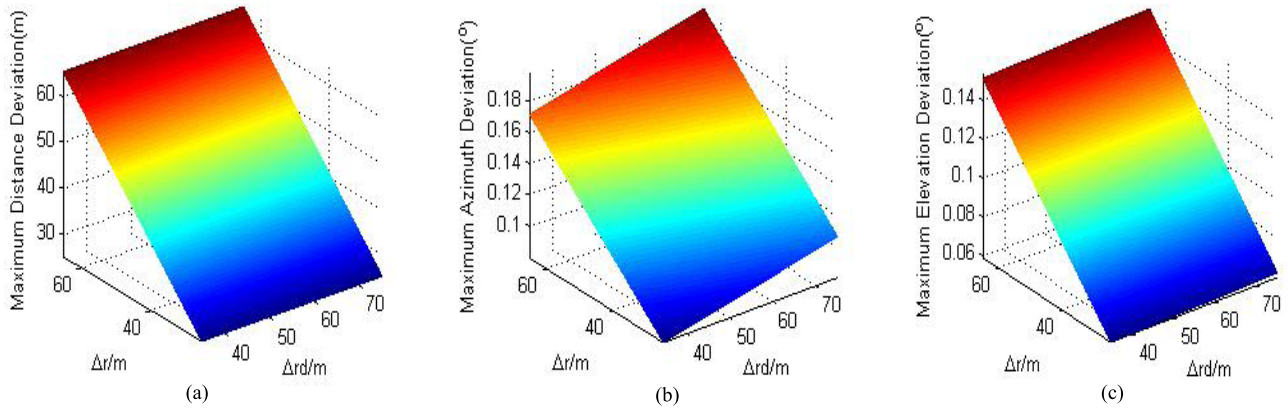

FIGURE 16. Variations of the ΔR_{max}, $\Delta\theta_{max}$, $\Delta\phi_{max}$ with the changes of Δr and Δrd. (a) Variations of the ΔR_{max}. (b) Variations of the $\Delta\theta_{max}$. (c) Variations of the $\Delta\phi_{max}$.

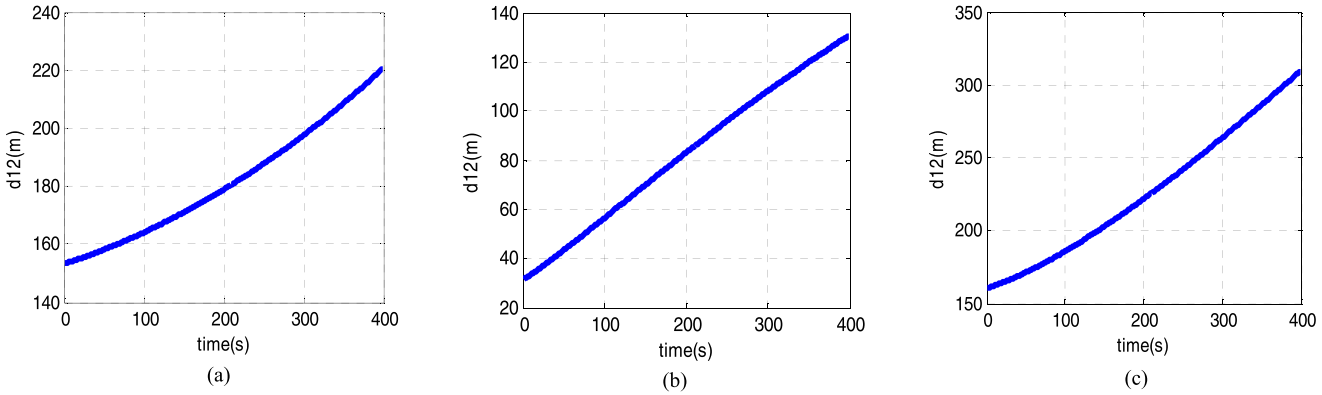

FIGURE 17. Variation of the d_{12}. (a) $\Delta r = 50m$. (b) $\Delta rd = 60m$. (c) $\Delta r = 50m$, $\Delta rd = 60m$.

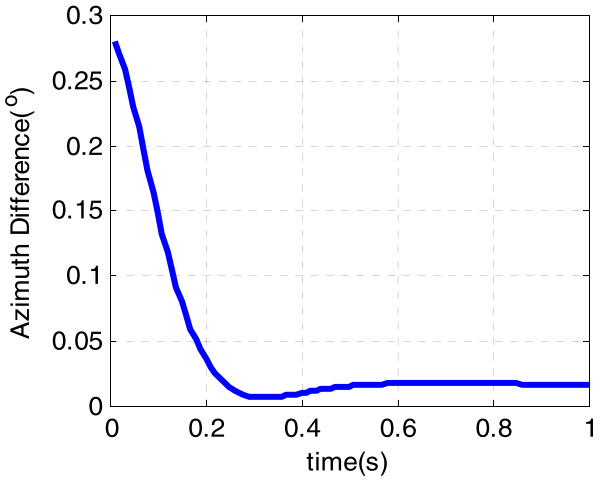

FIGURE 18. Variation of the $\theta_T - \theta_E$.

threshold $D_\alpha = 18.548$, when $\alpha = 0.005$, $n_Z = 6$. The value of N/M is selected by 4/5 and 7/10. Two sets of equal-length state samples are chosen at 70 and 35 seconds respectively. The tracks association detection results are shown in Table 1, after simulation with 100 trials.

TABLE 1. The tracks association detection results.

N/M	The probability of the phantom track passes the detection	The probability of the phantom track not passes the detection
4/5	0.11%	0.89%
7/10	0.05%	0.95%

Referring to Table 1, the probability of the phantom track not passes the detection means that the radar network can differentiate the phantom track. And we can denote it in P_D (probability of differentiation). What ECAVs want is minimize P_D.

From the results in Table 1, it can be seen that the phantom tacks can be differentiated well by using the tracks association detection. But it has a higher P_D when the value of N/M is 7/10 than 4/5. It is easy to understand that the more data samples for tracks association detection, the higher P_D will be achieved. It should be noted that as the data samples increases, the amount of calculation also increases. When we take the N/M value, the above factors need to be considered comprehensively.

The deviation compensation to the angle deviation mentioned in Section IV is used here. Two simulation scenarios are considered.

(a) The inaccuracy in position $\Delta r = 50\ m$, and Δrd increase from 40 m to 80 m.
(b) The inaccuracy in position $\Delta rd = 60\ m$, and Δr increase from 30 m to 70 m.

The value $N/M = 4/5$, two sets of equal-length state samples are chosen both from the 70 s. Simulation with 100 trials, the results of tracks association detection comparisons with/without deviation compensation control are shown in Fig. 19 and Fig. 20.

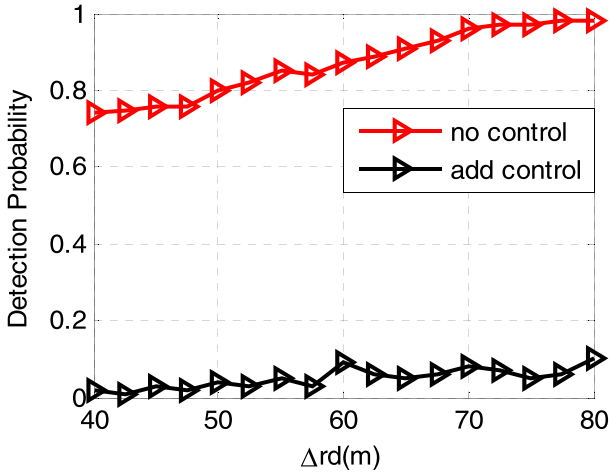

FIGURE 19. Variation of detection probability with Δrd.

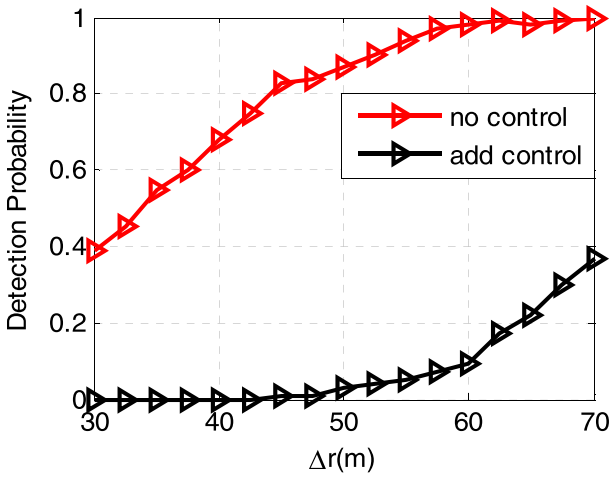

FIGURE 20. Variation of detection probability with Δr.

From the simulation results shown in Fig. 19 and Fig. 20, it can be seen that when no control command is added, the distributed radar network can easily recognize the phantom tracks target. The uncertainty in position is bigger, the better of the result of recognition. When the control command is added, the detection probability of phantom tracks target P_D drops rapidly.

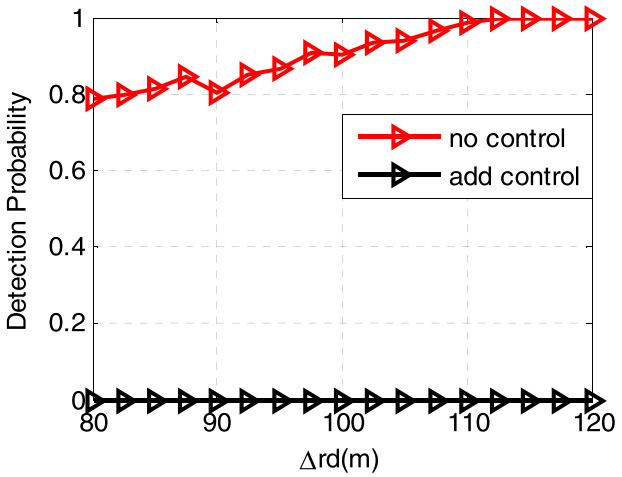

FIGURE 21. The relationship between detection probability and Δrd.

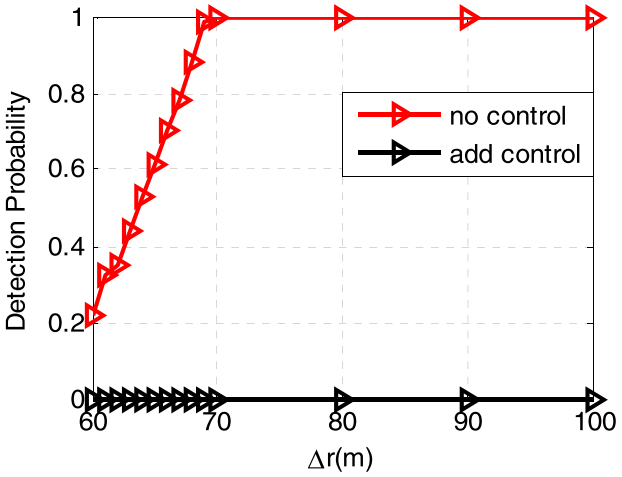

FIGURE 22. The relationship between detection probability and Δr.

The same two simulation scenarios are considered in same source testing used by centralized radar network [22]. Two sets of equal-length state samples are chosen both from the 50 s. Simulation with 500 trials, the results of same source testing comparisons with/without deviation compensation control are shown in Fig. 21 and Fig. 22.

Comparing Fig. 19, 20 with Fig. 21, 22, we can see that when no control command is added, the distributed and centralized radar network both can recognize the phantom tracks target easily. In addition, the deviation compensation can be used in distributed and centralized radar network. The deviation compensation method can reduce the recognition rate of the phantom track effectively in two different fusion architectures. And it works better in a centralized radar network.

VI. CONCLUSIONS

In this paper, a deviation compensation for phantom radar tracks is proposed, which is based on two kinds of phantom tracks in 3-D space. The effect of the inaccuracies of radar

position and ECAVs position to the phantom track is considered in detail. The simulation shows that the phantom target associated distance d_{12} is not only related to the distance R and r, but also related to the inaccuracy in position Δr and Δrd. Furthermore, it is mainly determined by the value of Δr. Through the deviation compensation to the angle deviation, which can reduce the recognition rate of the phantom track effectively.

REFERENCES

[1] G. Wang and Z. Ji, "Multi-range-false-target jamming for radar network based on multiple discriminations," *Syst. Eng. Electron.*, vol. 39, no. 1, pp. 40–48, Jan. 2017.

[2] C. Yang, L. Feng, H. Zhang, S. He, and Z. Shi, "A novel data fusion algorithm to combat false data injection attacks in networked radar systems," *IEEE Trans. Signal Inf. Process. Netw.*, vol. 4, no. 1, pp. 125–136, Mar. 2018.

[3] B. Rao, S. Xiao, X. Wang, and T. Wang, "Maximum likelihood approach to the estimation and discrimination of exoatmospheric active phantom tracks using motion features," *IEEE Trans. Aerosp. Electron. Syst.*, vol. 48, no. 1, pp. 794–819, Jan. 2012.

[4] C. Yang, H. Zhang, F. Qu, and Z. Shi, "Secured measurement fusion scheme against deceptive ECM attack in radar network," *Secur. Commun. Netw.*, vol. 9, no. 16, pp. 3911–3921, Nov. 2016.

[5] S. Zhao, L. Zhang, Y. Zhou, N. Liu, and J. Liu, "Discrimination of active false targets in multistatic radar using spatial scattering properties," *IET Radar, Sonar Navigat.* , vol. 10, no. 5, pp. 817–826, 2016.

[6] F. Li, Z. L. Zhou, X. Y. Gou, and Z. Q. Chen, "Phantom track generation using coherent dual moving sources for monopulse radar," *Syst. Eng. Electron.*, vol. 35, no. 11, pp. 2309–2313, Nov. 2013.

[7] Y.-R. Zhang, Y.-J. Li, and M.-G. Gao, "Performance analysis of typical mean-level CFAR detectors in the interfering target background," in *Proc. ICIEA*, Hangzhou, China, 2014, pp. 1451–1455.

[8] M. Pachter, P. Chandler, R. Larson, and K. Purvis, "Concepts for generating coherent radar phantom tracks using cooperating vehicles," in *Proc. AIAA Guid., Navigat., Control Conf. Exhibit*, Providence, RI, USA, 2004, pp. 1–14.

[9] B. P. Keith, P. R. Chandler, and M. Pachter, "Feasible flight paths for cooperative generation of a phantom radar track," *J. Guid., Control Dyn.*, vol. 29, no. 3, pp. 653–661, May/Jun. 2006.

[10] D. H. A. Maithripala and S. Jayasuriya, "Radar deception through phantom track generation," in *Proc. Amer. Control Conf.*, Portland, OR, USA, 2005, pp. 4102–4106.

[11] D. H. A. Maithripala and S. Jayasuriya, "Phantom track generation in 3D through cooperative control of multiple ECAVs based on geometry," in *Proc. 1st Int. Conf. Ind. Inf. Syst.*, Peradeniya, Sri Lanka, 2006, pp. 255–260.

[12] I.-H. Lee and H. Bang, "A cooperative line-of-sight guidance law for a three-dimensional phantom track generation using unmanned aerial vehicles," *Proc. Inst. Mech. Eng. G, J. Aerosp. Eng.*, vol. 227, no. 6, pp. 897–915, May 2016.

[13] I.-H. Lee and H. Bang, "Optimal phantom track generation for multiple electronic combat air vehicles," in *Proc. Int. Conf. Control, Automat. Syst.*, Seoul, South Korea, 2008, pp. 29–33.

[14] Y. Xu and G. Basset, "Virtual motion camouflage based phantom track generation through cooperative electronic combat air vehicles," in *Proc. Amer. Control Conf.*, Baltimore, MD, USA, 2010, pp. 5655–5661.

[15] Y. Zhao, Y. Chen, J. Meng, and H. Dong, "A data processing method against multi-false-target deception jamming for distributed radar network," *Electron. Opt. Control*, vol. 18, no. 3, pp. 25–30, Mar. 2011.

[16] D. C. He, G. H. Wang, and D. X. Sun, "Target tracking technique for distributed radar network under distributed jamming," *Mod. Defence Technol.*, vol. 44, no. 4, pp. 81–88, Aug. 2016.

[17] D. Sun, W. Guohong, and Z. Xiangyu, "Algorithm of discriminating phantom track and target track for radar network based on multivariate statistical analysis theory," *Acta Electron. Sinica*, vol. 42, no. 9, pp. 1680–1685, Sep. 2014.

[18] A. Ratnoo and T. Shima, "Formation-flying guidance for cooperative radar deception," *J. Guid., Control Dyn.*, vol. 35, no. 6, pp. 1730–1739, Nov. 2012.

[19] D. Narayanachar, A. Kuduvalli, and D. Ghose, "Generation of a class of proportional navigation guided interceptor phantom tracks," *J. Guid., Control Dyn.*, vol. 38, no. 11, pp. 2206–2214, Nov. 2015.

[20] D. X. Sun, G. H. Wang, and D. Sheng, "Phantom track jamming recognition based on mean-covariance collaborative testing," *Acta Aeronaut. Astronaut. Sinica*, vol. 37, no. 4, pp. 1292–1304, Apr. 2016.

[21] G. H. Wang, Z. Yang, and J. P. Wu, "Influence analysis of radar location error on multi-aircraft cooperative track deception," *J. Naval Aeronaut. Astron. Univ.*, vol. 30, no. 6, pp. 501–504, Jun. 2015.

[22] X. Liu and D. Li, "The technology of deviation compensation for radar phantom tracks," in *Proc. ICCT*, Chengdu, China, 2017, pp. 1098–1101.

[23] P. Zarchan, *Tactical and Strategic Missile Guidance*, 2nd ed. Washington, DC, USA: AIAA, 1994.

[24] N. Dhananjay, A. Kuduvalli, and D. Ghose, "Realistic coherent phantom track generation by a group of electronic combat aerial vehicles," in *Proc. Amer. Control Conf.*, Washington, DC, USA, 2013, pp. 4642–4647.

[25] X. R. Li, Y. Zhu, J. Wang, and C. Han, "Optimal linear estimation fusion—Part I: Unified fusion rules," *IEEE Trans. Inf. Theory*, vol. 49, no. 9, pp. 2192–2208, Sep. 2003.

[26] H. Fourati and K. Iniewski, *Multisensor Data Fusion: From Algorithms and Architectural Design to Applications*. Boca Raton, FL, USA: CRC Press, 2016.

XIANG LIU is currently pursuing the Ph.D. degree in signal processing with the College of Electronic Engineering, National University of Defense Technology, Hefei, China. His research interests include radar signal processing, information fusion in multisite radar systems, and radar electronic countermeasure.

DONGSHENG LI received the Ph.D. degree from the Hefei University of Technology, Hefei, China, in 2011. He is currently a Professor with the National University of Defense Technology. His research interests include radar signal processing and electromagnetic environment effects.